Available online at www.joac.info

ISSN: 2278-1862

Journal of Applicable Chemistry

2016, 5 (4): 738-750

(International Peer Reviewed Journal)

High Surface Area, Mesoporous, Poorly Crystalline MnO_2 with High Na^+ Ion Insertion Capacity

Brij Kishore[1], Venkatesh Gopal[2] and Munichandraiah Nookala*[1]

1. Department of Inorganic and Physical Chemistry, Indian Institute of Science, Bangalore - 560012, **INDIA**
2. Department of Instrumentation and Applied Physics, Indian Institute of Science, Bangalore - 560012, **INDIA**

Email: muni@ipc.iisc.ernet.in

Accepted on 13th June 2016

ABSTRACT

Poorly crystalline or amorphous MnO_2 is prepared by the redox reaction between aqueous solutions of $KMnO_4$ and $MnSO_4.H_2O$ at ambient conditions. The as prepared sample obtained by drop-wise addition of $KMnO_4$ solution to $MnSO_4$ solution has a specific surface area as high as 184 m^2 g^{-1} with narrowly distributed mesopores of 3.5 nm pore diameter. However, there is an increase in crystallinity into the α-form and a decrease in specific surface area with an increase in temperature, when the amorphous MnO_2 samples are heated up to 800 °C. Na/MnO_2 cells are assembled in propylene carbonate electrolyte consisting of $NaClO_4$. The as prepared sample provides the first discharge capacity of 194 mAh g^{-1} at a specific current of 50 mA g^{-1}. The attractively high discharge capacity of the as prepared amorphous MnO_2 is attributed to the large specific surface area and mesoporosity. There is a decrease in specific discharge capacity on subjecting the cells to repeated charge-discharge cycling. A discharge capacity of about 70 mAh g^{-1} is obtained at the end of 30 charge-discharge cycles. The initial discharge capacity values of crystalline α-MnO_2 samples are lower than the amorphous samples, but with improved cycling stability.

Keywords: mesoporous MnO_2; poor crystallinity; Na-ion cells; high capacity.

INTRODUCTION

Research activities on Na-ion batteries have become intensive in the recent years, because these batteries, if successfully developed, are considered as economical alternatives to Li-ion batteries [1-3]. Although, the use of small size Li-ion batteries is now wide spread over important portable applications such as cellular phones, laptop computers and camcorders, their range of applications is expected to increase in larger sizes for applications such as electric vehicles in future. One of the major concerns for expansion of Li-ion batteries in large sizes is the limited and unevenly distributed global resources of Li and therefore its high cost. As the sources of Na are distributed over the globe in plentiful and also Na is significantly cheaper than Li, research and development activities are now diverted towards Na-ion batteries. Although Li and Na have many similarities in chemical properties, differences in properties such as electrode potentials (-2.71 V for Na versus -3.05 V for Li), ionic radii (1.02 Å for Na versus 0.76 Å for Li), etc. play important role in deciding the inferior performance of the proposed Na-ion cells to the already well-developed Li-ion

cells. Nevertheless, the low cost and plentiful global availability of Na overweigh the limitations of Na-ion cells and they are expected to be useful, when commercially developed, for applications next to Li-ion cells.

Research activities on various electrode materials for Na-ion cells run almost parallel to those of Li-ion cells. In the several known electrode materials of Li-ion cells, Li is replaced by Na in the synthetic procedures, and the sodiated compounds are investigated for Na-ion cells [4-6]. Among the positive electrode materials, transition metal oxides are studied extensively [7-9]. Manganese based oxides are important as Mn is inexpensive and chemistry as well as electrochemistry of various Mn oxides are studied well and reported in the literature [10-12]. The electrochemistry of MnO_2 is popular ever since the discovery of Zn-MnO_2 Leclanche cells.

For the studies in Na-ion cells, sodiated manganese oxide (Na_xMnO_2) was prepared by combustion route using glycine as the fuel and cycled against Na as the negative electrode in a polymer electrolyte medium [13]. Samples of $Na_{0.44}MnO_2$ were treated with dil. HCl solution to remove mobile Na^+ ions and Mn_2O_3 impurities, capacities of the resultant compounds were measured in the composition range $0.2 < x < 0.75$. At $x > 0.75$, there was a difficulty in passing current. The mechanism of insertion/deinsertion processes of Na^+ in Na_xMnO_2 was studied by low rate cycling in a solution of 1 M $NaClO_4$ in propylene carbonate [14]. Six distinct biphasic phenomena were reported within $0.18 < x < 0.64$ composition range of Na_xMnO_2. Nanostructures of α- and β- polymorphs of MnO_2 were prepared by hydrothermal route and studied as negative electrode materials for Na-ion batteries [15]. It was reported that β-MnO_2 exhibited greater Na^+ ion storage capacity than α-MnO_2.

The performance of various electrode materials thus far studied for Na-ion cells is not comparable with the performance of electrode material developed for Li-ion cells. The larger size of Na^+ ion in comparison with Li^+ ion appears to be responsible factor. A facile diffusion of Na^+ ions in amorphous frameworks is expected to result in improved performance of charge/discharge cycling involving intercalation/ deintercalation of Na^+ ions. Thus, focus has shifted towards amorphous electrode materials for Na-ion batteries, recently. Amorphous TiO_2 nanotube array is reported as high capacity stable anode material for Na-ion batteries [16]. Amorphous sodium vanadate is reported to have cycling stability at 1.8 V vs. Na/Na^+ with a discharge capacity of 150 mAh g^{-1} [17]. Amorphous V_2O_5 with a discharge capacity of 241mAh g^{-1} is shown better than crystalline oxide with a discharge capacity of 120mAh g^{-1} [18]. Amorphous $FePO_4$ with mesoporosity is reported to provide a high initial discharge capacity, stable cyclability and high rate capability [19]. It is reported that hollow amorphous $NaFePO_4$ nanospheres provide a high discharge capacity as well as high rate capability [20]. There are no reports on electrochemical behaviour of amorphous MnO_2 in Na^+ ion based non-aqueous electrolytes. Studies on electrochemical properties of high surface area, mesoporous and amorphous MnO_2 are reported in the present work. An initial discharge capacity as high as 194 mA h g^{-1} in Na^+ ion electrolyte is obtained against a general observation that a well crystalline form is necessary for insertion of Na^+ ion in MnO_2. When the amorphous MnO_2 is converted into a crystalline form by heating at high temperatures, there is a decrease in the initial Na^+ ion insertion capacity.

MATERIALS AND METHODS

All chemicals of analytical grade were used as received. They included $KMnO_4$ (SRL), $MnSO_4.H_2O$ (HIMEDIA), acetylene black (AB, 99.9% Alfa Aesar), polytetrafluoroethylene (PTFE) suspension (Aldrich), hexane (SDFCL), $NaClO_4$ (Aldrich), Na metal lumps (SDFCL) and propylene carbonate (PC, Aldrich). A sodium lump was washed in hexane to remove paraffin oil and thin slices were made for using as reference cum counter electrode in a two electrode-cell configuration. All aqueous solutions were prepared in double distilled (DD) water.

Synthesis: MnO_2 was synthesized by redox reaction between $KMnO_4$ and $MnSO_4$ [21]. In brief, 0.727 g of $KMnO_4$ was dissolved in 50 mL of DD water and added drop wise to 50 mL aqueous solution containing

1.166 g of $MnSO_4.H_2O$ under constant stirring. After the complete addition, the contents were stirred for additional 6 h. The product was collected by filtration, washed copiously with DD water, then with ethanol and dried at 70 ^oC for about 12 h. The as synthesized sample is referred to as S70. The quantity of sample prepared in each batch was typically 1.0 g. Several batches of preparation were carried out and the product samples were mixed together. Portions of it were heated at various temperatures between 300 and 800 °C for 6 h. The samples, which were heated at 300, 400, 500, 600, 700 and 800 ^oC are referred to as S300, S400, S500, S600, S700 and S800, respectively.

Characterization: The MnO_2 samples were characterized by powder X-ray diffraction (XRD) using a Philips X'Pert Pro diffractometer at 40 kV and 30 mA with Cu K_α (λ=1.5418 Å) as the radiation source and the data were collected at 2θ range from 10 to 90^o at a rate of 2^o per min. The morphology was examined using a FEI Co scanning electron microscope (SEM) model Sirion. Nitrogen adsorption-desorption isotherms were recorded at -196 ^oC using Micromeritics surface area analyzer model ASAP2020. The specific surface area was calculated by the Brunauer-Emmett-Teller (BET) method from the adsorption branch. The pore size distribution was calculated by Barrett-Joyner-Halenda (BJH) method from desorption branch of the isotherm. The oxidation states of Mn on the surface of the sample was examined by high resolution X-ray photoelectron spectroscopy (XPS: Kratos Axis Ultra DLD system) with dual Al source of 1486.6 eV, 300 μm × 700 μm aperture size. The stoichiometry was checked via Inductively Coupled Plasma-Optical Emission Spectrometry (ICP-OES) with a Perkin Elmer Optima 2100DV Analytical Instruments.

Electrochemical measurements: For fabrication of electrodes, the active material (70wt%), AB (20 wt%) and PTFE suspension (10 wt%) were mixed in a mortar and ground well. The dough, thus, formed was rolled into a sheet on a glass plate. Stainless steel (SS) mesh of 0.3 mm thickness and mesh size 80 was used as the current collector. The pre-treatment of SS mesh was carried out by first etching it in 5 N HCl solutions, followed by etching in 5 N HNO_3. It was then washed thoroughly with DD water, rinsed with acetone and air dried. The rolled sheet of electrode material was transferred onto a mesh of 12 mm diameter such that the loading level of the active material was 9 – 12 mg cm^{-2}. The electrodes were then dried at 100^{o}C under reduced pressure for 12 h. For electrochemical studies, a home-made Swagelok-type cell assembly was used where Na metal foil (12 mm diameter) was used as the counter cum reference electrode and an absorbent glass mat (AGM) as the separator. The electrolyte used was 1 M $NaClO_4$ in PC. Swagelok cells were assembled in argon filled MBraun glove box model Unilab. Cyclic voltammetry, charge-discharge cycling experiments and rate capability with different currents was carried out using a Biologic multi-channel potentiostat/galvanostat model VMP3.All experiments were carried out at 22±1 ^oC.

RESULTS AND DISCUSSION

Synthesis: There are various synthetic routes for the preparation of MnO_2, which include oxidation of Mn^{2+} ions by a suitable oxidizing agent, reduction of Mn^{7+} by a reducing agent and electrochemical deposition. In the present study, the synthesis of MnO_2 was carried out by adding drop-wise a neutral aqueous solution of $KMnO_4$ to an aqueous solution of $MnSO_4$. The redox reactions between Mn^{+7} and Mn^{+2} result in the formation of MnO_2 [21].

$$2\ KMnO_4 + 3\ MnSO_4 + 2\ H_2O \longrightarrow 5\ MnO_2 + K_2SO_4 + 2\ H_2SO_4 \quad (1)$$

The reaction was carried out at room temperature. The product was washed and dried at 70 °C (sample S70). The as synthesized samples were further heated at various temperatures ranging from 300 – 800 °C (samples S300 - S800).

There are several reports on synthesis of MnO_2 from the redox reaction between Mn^{2+} and Mn^{7+} ions [22 – 25]. DeGuzman *et al.,* [22] prepared MnO_2 of different crystal phases by varying pH and temperature from the redox reaction between $KMnO_4$ and $MnSO_4$. Chen *et al.,* [23] prepared α-MnO_2 from $KMnO_4$ and H_2SO_4 at 70 – 95 °C by the redox reaction between Mn^{7+} and Mn^{2+}, the latter being formed by reduction of

$KMnO_4$ in strong acidic conditions. In a hydrothermal synthesis, α- and β- phases of MnO_2 were obtained by redox reaction between $KMnO_4$ and $MnSO_4$ under hydrothermal conditions at 160 °C for durations of 8 and 72 h, respectively [24]. Crystalline MnO_2 nanoparticles were prepared by mixing aqueous solutions of $KMnO_4$ and $MnSO_4$ at ambient conditions and aging for different durations at 25 and 85 °C [25]. It is understood from the above reports that the redox reaction between $KMnO_4$ and $MnSO_4$ produces different crystalline phases by varying the reaction conditions. Unlike the formation of crystalline phases of MnO_2 in these reports, an amorphous MnO_2 is obtained in the present study from the reaction between aqueous solutions of $KMnO_4$ and $MnSO_4$, as detailed below. The formation of amorphous MnO_2 is attributed to a drop-wise addition of $KMnO_4$ solution to $MnSO_4$ solution.

The S70 and S800 samples were subjected to chemical analysis by ICP and also to Thermogravimetry. There is a loss of 11.29 wt% when S70 sample was subjected to Thermogravimetry at 250 °C. The results of chemical analysis after applying correction of 11.29 wt% water is Mn 60.32, K 1.47, and O 33.90 wt%. Thus the composition of S70 sample becomes $MnK_{0.033}O_{2.17}$. Similarly, from Mn 64.43% and O 35.57 %, the composition for S800 sample becomes $MnO_{1.9}$.

XRD and XPS studies: Powder XRD patterns of MnO_2 samples are shown in Fig. 1. The XRD patterns (Fig. 1, (i), (ii) and (iii)) of the samples S70, S300 and S400 are poorly crystalline. Minor broad peaks are observed at 2θ values of 36.6°, 41.1°, 54.7° and 65.9° corresponding to the α-phase [26, 27]. The XRD patterns of the samples S500, S600, S700 and S800, indicate well crystalline α-MnO_2 phases and they are indexed to JCPDS No. 44-0141. It is known that MnO_2 forms in different polymorphs depending on the way MnO_6 octahedra are inter-linked [27, 28]. For α-MnO_2, the octahedra are linked at the corners to form a (2 x 2) and a (1 x 1) channels. This structure allows the Na^+ ion diffusion. It has been reported that the K^+ ions originating from $KMnO_4$ partially occupy the tunnels, which serve to stabilize the tunnel structure of MnO_2 [29].

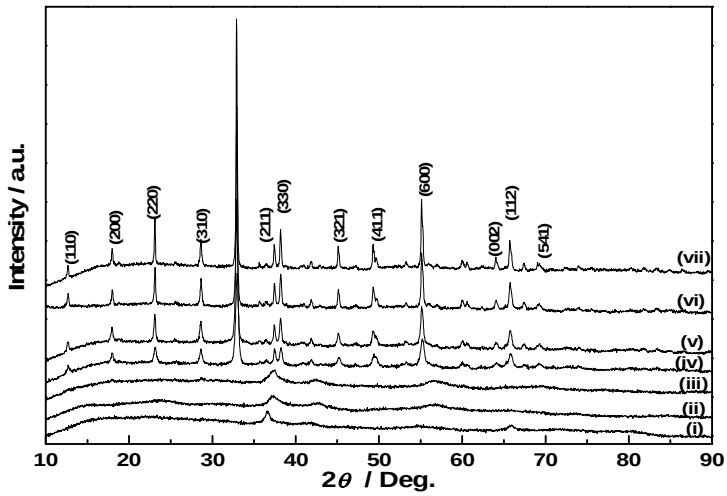

Fig. 1 XRD patterns for MnO_2 samples (i) S70, (ii) S300, (iii) S400, (iv) S500, (v) S600 (vi) S700 and (vii) S800.

The XPS spectrum for Mn $2p_{3/2}$ signal of the sample S70 is shown in Fig. 2. The spectrum is deconvoluted similar to procedure reported [30]. Oxidation states of Mn as +2, +3 and +4 are identified, but the major oxidation state is +4.

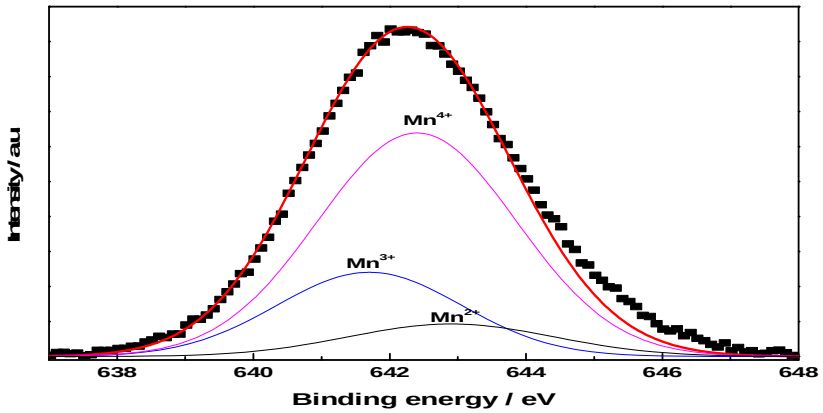

Fig. 2 Mn $2p_{3/2}$ XPS spectrum and deconvoluted curves for Mn^{2+}, Mn^{3+} and Mn^{4+} after background subtraction of as prepared MnO_2 sample (S70).

Morphology studies: Morphology of various MnO_2 samples was examined by SEM (Fig. 3). The morphology of sample S70 is like rough globules (Fig. 3a). Similar morphology is observed for S300 and S400 samples also (Fig. 3b and c). The effect of heating up to 400 °C is negligibly small on the morphology. But changes are clearly observed in the morphology of S500 sample (Fig. 3d). The rough globules are broken down into smaller spherical particles. The inter-particle spacing appear as pores. Formation of particles of size smaller than 200 nm is clearly seen for the sample heated at 600 °C (Fig. 3e). For the sample heated at 700 °C, several particles are fused with one another resulting in a worm-like structure (Fig. 3f). There is an increase in the extent of fusion of particles by heating the sample at 800 °C (Fig. 3g).

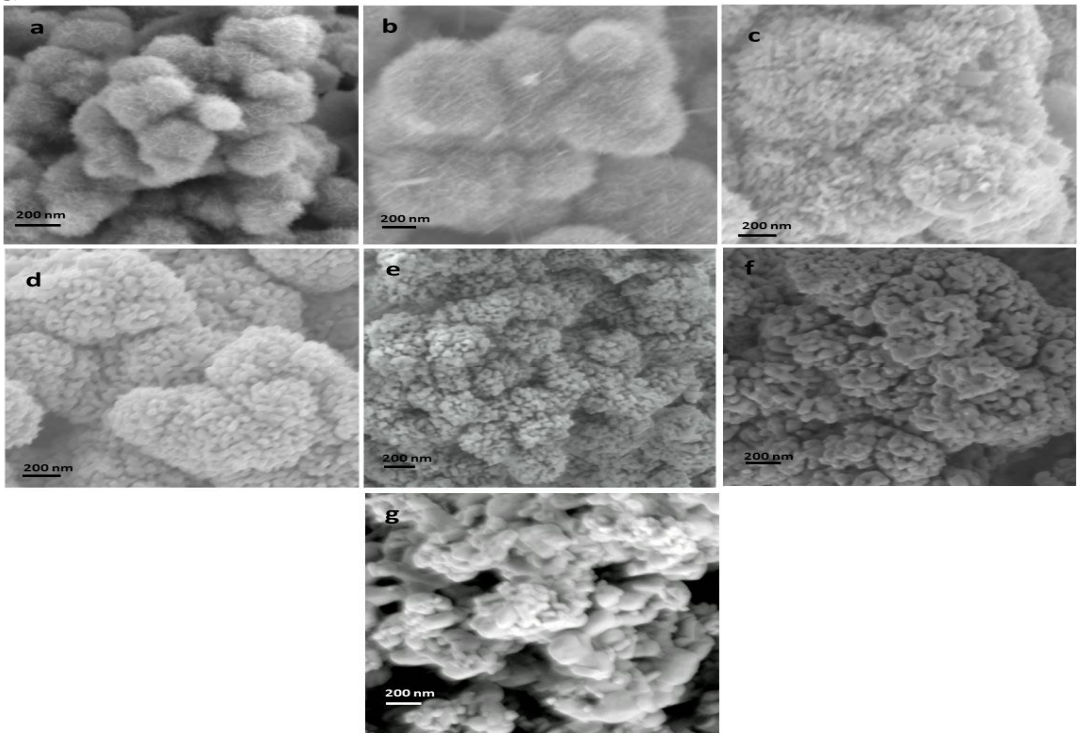

Fig. 3. SEM images of MnO_2 samples: (a) S70, (b) S300, (c) S400, (d) S500, (e) S600, (f) S700 and (g) S800.

BET surface area and porosity measurement: Nitrogen adsorption/desorption isotherms and BJH curves of various MnO_2 samples are shown in fig. 4. BET surface area and pore properties are listed in Table 1. There is a wide hysteresis loop in isotherm of the as prepared (S70) sample (Fig. 4a), which is an indication of porous nature of the sample. The BET specific surface area for the sample is 184m^2 g^{-1}. The BJH curve (Fig 4a inset), shows a very narrow pore size distribution at pore diameter of 3.5 nm. Similar BET isotherms are observed for samples S300 and S400 (Fig 4b and c), except for smaller hysteresis loops when compared with the as prepared sample. Furthermore, there is a decrease in surface area of S300 and S400 samples to 145 and 121 m^2 g^{-1}, respectively, in comparison with S70 sample (Table 1). The BJH pore size distribution curves of these two samples are interesting. Sample S300 exhibits an intense narrow distribution at 3.5 nm similar to the sample S70 and also another relatively broader pore size distribution at 4.7 nm (Fig. 4b inset). Thus, there is a gradual increase in pore diameter by heating the as prepared MnO_2 sample at 300 °C. In order to examine the effect of heating time on the nature of pore-size distribution, samples of S70 were heated at 300 °C for different durations from 1 to 10 h. The adsorption/desorption isotherms, BET surface area and BJH curves recorded for all samples (not shown) were found to be the same as shown in Fig. 4b for S300 sample prepared at 300 °C for 6 h. These results suggested the absence of any effect of heating time on sample (Fig. 4c). The 3.5 nm pore becomes less intense, and a broader pore distribution at 6.0 nm increases. There is a considerable decrease in the loop between adsorption and desorption isotherms of S500 sample (Fig. 4d). The BJH curve (Fig. 4d inset) indicates a narrow pore-size distribution at a pore diameter of about 25 nm. Thus, the 3.0 nm pore present in the as prepared sample (Fig. 4a inset) are converted into about 25 nm (Fig. 4d inset) by heating at 500 °C. Additionally there is a considerable decrease in pore volume as well as surface area (Table 1). The trends of decreasing BET surface area, increasing average pore diameter and decreasing pore volume exist for all samples heated up to 800 °C (Fig. 4e-g and Table 1). It is observed that samples heated at temperature ≥ 500 °C, the values of BET specific surface area and cumulative pore volume decreases significantly and the average pore diameter increases considerably. This could be ascribed to an increase in crystallinity on heating the samples at ≥ 500 °C.

Table 1: Specific surface area, average pore diameter, and cumulative pore volume of the various prepared heated and soaked samples.

Sample	Specific surface area (m^2 g^{-1})	Average pore diameter (nm)	Cumulative pore volume (cm^3 g^{-1})
S70	184	3.5	0.309
S300	145	5.9	0.301
S400	121	6.9	0.292
S500	34	24.2	0.236
S600	20	36.4	0.167
S700	13	45.9	0.046
S800	7	46.5	0.014
Soaked-S70	148	5.2	0.306

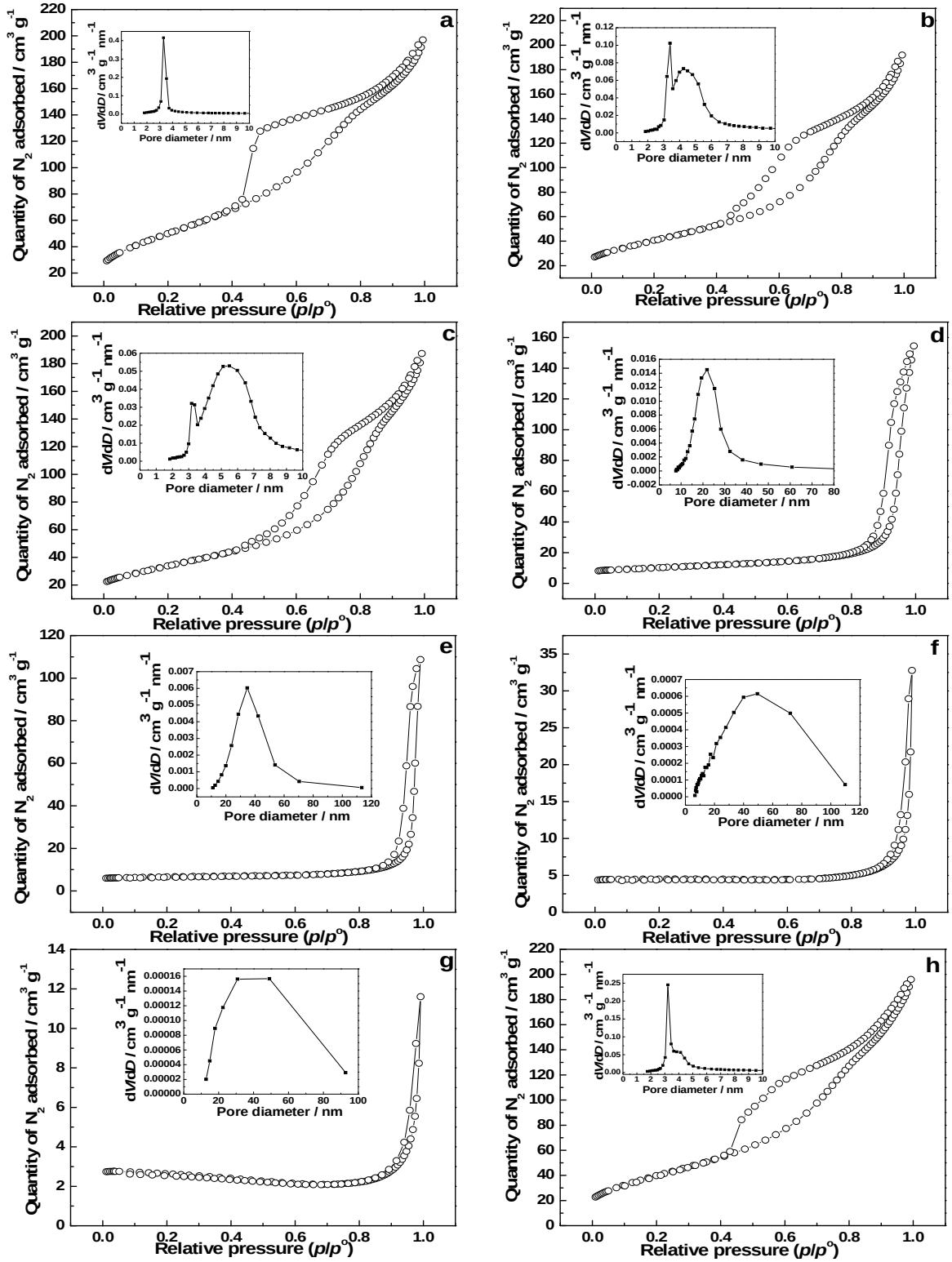

Fig. 4. Nitrogen adsorption/desorption isotherms of MnO_2 samples: (a) S70, (b) S300, (c) S400, (d) S500, (e) S600, (f) S700, (g) S800 and (h) soaked-S70. BJH pore size distribution is shown in inset for respective samples.

Electrochemical measurements: Cyclic voltammograms of Na/MnO_2 cells employing S70 sample were recorded in cell voltage range 1.0 – 4.3 V at a sweep rate of 0.05 mV s^{-1} (Fig. 5a). In the cathodic sweep, starting at 3.30 V, a current peak (P_c) is observed at 2.08 V, which is due to the reduction of Mn^{+4} accompanying the insertion of Na^+ ions. In the reverse direction, a small oxidation peak (P_{a1}) observed at 2.65 V and another minor peak (P_{a2}) at 3.88 V appear in the first cycle. However, the intensity of peak P_{a1} decreases, whereas that of P_{a2} increases markedly in the second cycle. Similar voltammograms were recorded for all samples. The current peak P_c is attributed to insertion of Na^+ ion followed by the reduction of Mn^{4+} and the peak P_{a2} to deinsertion of Na^+ ions. The reaction corresponding to sodiation/desodiation of Na^+ in MnO_2 is:

$$MnO_2 + x\,Na^+ + x\,e^- \rightleftarrows Na_xMnO_2 \qquad (2)$$

Voltage profiles of all Na/MnO_2 cells during the first Galvanostatic discharge/charge cycling are shown in Fig. 5b. Since MnO_2 is present in the charged state, the electrodes were first discharged to 1.0 V and then charged to 4.3 V at a cell current of 500 µA (23 mA g^{-1}). During discharge of the cell with S70 sample, voltage plateaus are not clearly visible (Fig. 5b(i)). However, two voltage plateaus are clearly observed in the charging voltage profile. Voltage plateaus during both discharge and charge are clearly seen as peaks in differential plots (Fig. 5b inset). There are two peaks observed at 2.0 and 1.3 V, indicating a two-stage insertion of Na^+ ions into MnO_2 during the discharge. These peaks are clearly observed in the differential plot (Fig. 5b inset). Although there is lack of clarity in the voltage plateaus in discharge profiles (Fig. 5b) and only single broad current peak is observed in cyclic voltammograms (Fig. 5a). On the other hand clear voltage plateaus are observed during charging at 2.2 – 2.7 V and 3.2 – 3.7 V regions and the corresponding peaks in the differential plot are present at 2.5 and 3.3 V, respectively.

The appearance of clear voltage plateaus during charge against vague plateaus during discharge is likely due to differences in the kinetics of reactions. Diffusion of Na^+ ions during charge is ascribed to be slower than during discharge. A capacity of 194 mAh g^{-1} is obtained at current density of 50 mA g^{-1} in the second discharge of S70 sample. Similar to the behaviour of S70 sample, S300-S800 samples also exhibit two stages of charge and discharge but with different capacity values (Fig. 5(ii-vii)). The values of capacity obtained in the second discharge of Na/MnO_2 cells with MnO_2 samples S70, S300, S400, S500, S600, S700 and S800 are 194, 196, 191, 70, 49, 32 and 22 mAh g^{-1}, respectively, at a specific current density of 50 mA g^{-1}. The poorly crystalline S70, S300 and S400 samples provide the highest discharge capacity among all MnO_2 samples. Subsequent to the formation of crystalline samples at ≥ 500 °C, the discharge capacity decreases significantly. Furthermore, greater is the crystallinity the samples, lower is the discharge capacity.

It is generally believed that crystalline compounds are only useful for Li-ion batteries. A study of the literature reports, however, suggests that amorphous compounds are more interesting than the crystalline compounds in terms of superior cycling performance [31-34]. Kim and Manthiram [31] prepared amorphous lithiated manganese oxyiodide with a high reversible Li-ion capacity of 260 mAh g^{-1}. Although this compound had an average discharge voltage of 2.6 V, a high discharge capacity was expected to provide greater energy density than the conventional crystalline cathode materials. Xu *et al.*, [32] reported amorphous manganese oxides prepared by oxidation of Mn(II) precursors in aqueous solutions at ambient conditions and studied as Li intercalation chemistry. Leroux et al., [33], Palos *et al.*, [34] and Manthiram *et al.*, [35] synthesized different amorphous alkaline manganese oxides from aqueous solutions using various reducing agents and reported capacities in the range of 160 – 220 mAh g^{-1}. Capacity values greater than 400 mAh g^{-1} in a Li salt electrolyte were reported by Xu *et al.*, [36] for amorphous manganese dioxide synthesized from sodium permanganate by fumaric acid reduction. Amorphous Fe_2O_3 films were grown by electro spray deposition, which provided a charge-discharge capacity of 1600 mAh g^{-1} as a Li-ion battery anode material [37]. The out performance of amorphous Li-ion battery electrode materials in attributed to short range order of crystal structure, which is expected to overcome the problems associated with lattice distortion of well-crystalline structures. It is believed that

the increased discharge capacity of amorphous materials is due to the existence of smooth pathways in short range crystal order for the process of Li^+ insertion and extraction, thereby enhancing Li^+ diffusion rate and lowering the cell resistance [31]. In the present study, the high Na^+ ion intercalation/deintercalation capacity obtained from the large surface area amorphous MnO_2 is attributed to greater amount of Na^+ ions intercalated in short range of crystallographic lattice than in well crystalline samples. Furthermore, high porosity of the amorphous samples is expected to allow tolerance for volume expansion/contraction stresses that accompany Na^+ ion intercalation/deintercalation processes.

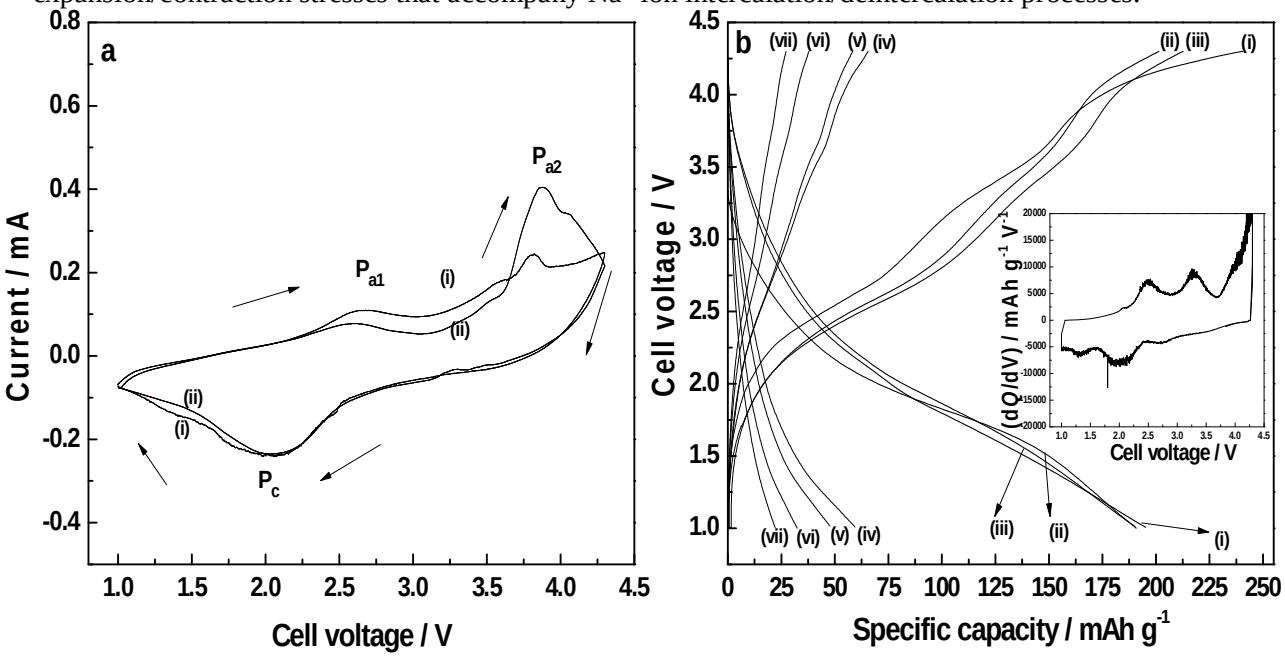

Fig. 5 (a) Cyclic voltammogram of MnO_2 sample (S70) at a sweep rate of 0.05 mV s^{-1} in the potential range of 1.0 – 4.3 V vs. Na/Na^+ and (b) 2nd cycle charge-discharge curves for various MnO_2 samples (i) S70, (ii) S300, (iii) S400, (iv) S500, (v) S600, (vi) S700 and (vii) S800 and inset of the graph is differential specific capacity curve for S70 sample.

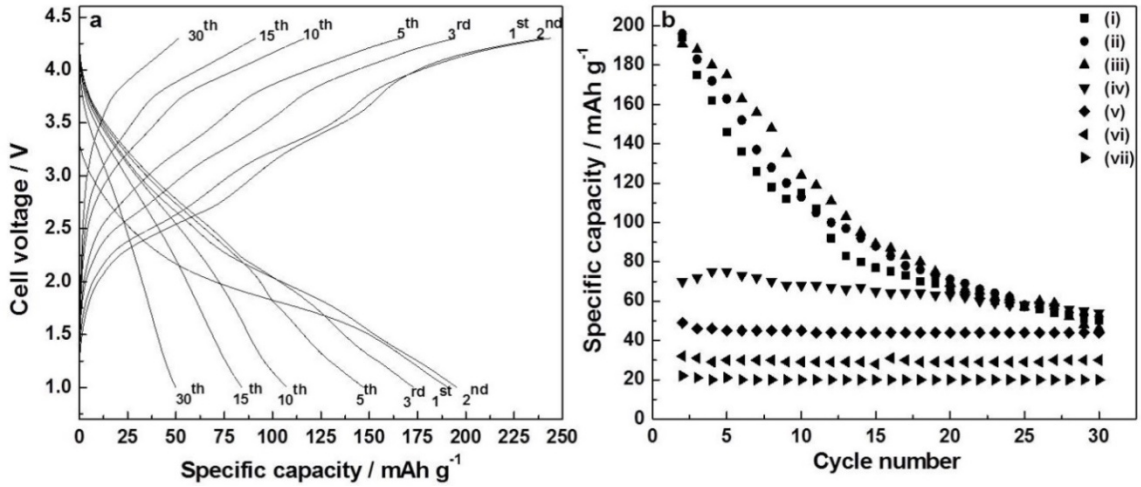

Fig. 6 (a) Galvanostatic charge-discharge curves for various cycles of MnO_2 sample (S70) at current density of 53 mA g^{-1} and (b) Cycle life for various MnO_2 samples: (i) S70, (ii) S300, (iii) S400, (iv) S500, (v) S600, (vi) S700 and (vii) S800. For cycle life tests, a current of 500 µA was used and loading level of the active material was 10 – 12 mg cm^{-2}.

All MnO_2 electrodes were subjected to cycle-life test at a specific current of 50 mA g^{-1}. Charge-discharge voltage profiles of S70 sample are shown in Fig. 7a. There is a gradual decrease in capacities of both charge and discharge on repeated cycling. The variation of discharge capacity is shown in Fig. 7b (i). The discharge capacity decreases fast from an initial value of 194 mAh g^{-1} to 80 mAh g^{-1} at the 20th cycle. The capacity is fairly constant between 20th and 30th cycles. The cycling behaviour of S300 and S400 is similar to the behaviour of S70 sample (Fig. 7b (ii) and (iii)). The cycling behaviour of samples S500 - S800, however, is different from the behaviour of S70 - S400 samples. The S500 - S800 samples provide stable capacity values from the beginning. The specific capacity of M500 sample is about70 mAh g^{-1} throughout the 30 charge-discharge cycles; whereas the stable discharge capacity values of S600, S700 and S800 samples are 40, 30 and 20 mAh g^{-1}, respectively.

The MnO_2 samples studied in the present work can be grouped into two categories: (i) poorly crystalline S70, S300 and S400 samples, and (ii) well crystalline S500, S600, S700 and S800 samples (Fig. 1). It is interesting to notice that poorly crystalline samples (S70 - S400) exhibit a high discharge capacity initially, but their capacity decreases rapidly within about 20 charge-discharge cycles (Fig. 7b (i)-(iii)). However, the second category of well crystalline samples provides low but steady discharge capacity throughout the 30 cycle test. Furthermore, the capacity decreases with an increase in temperature of preparation of crystalline samples (Fig. 7b (iv)-(vii)).

Synthesis of sodiated manganese oxides has been reported in the literature for Na-ion battery application. Among these oxides, $Na_{0.44}MnO_2$ has attracted attention as a cathode material because of its wide tunnel structure with theoretical capacity of 122 mAh g^{-1} and good cyclability [38]. Sauvage *et al.*, [14] prepared $Na_{0.44}MnO_2$ by solid state synthesis route and reported 80mAh g^{-1} for Na^+ ion insertion/extraction capacity. However, its cyclic stability was poor. Caballero et al., [6] reported an initial capacity of about 150 mAh g^{-1} which decreased to 74mAh g^{-1} after 10 cycles. The results of the present studies are similar to the observations reported in literature.

In addition to high discharge capacity (~200 mAh g^{-1}) obtained from S70 - S400 samples, a good cycling stability could have been desirable for application in Na-ion batteries. As the discharge capacity decreases significantly on repeated charge-discharge cycling, several possible factors responsible for the capacity fade are analyzed. It is observed from the charge-discharge voltage profiles of M70 sample over 30 cycles (Fig. 7a) that there is a gradual increase in charging voltage plateaus in addition to a decrease in capacity. This means kinetics of electrochemical processes gradually decreases leading to a decrease in electrochemical activity. In order to examine the effect of aging of the electrodes in Na^+ ion electrolytes, S70 electrodes were soaked in $NaClO_4$ + PC electrolyte in Ar atmosphere glove box for 7 days, cells were assembled and subjected to charge-discharge cycling. The electrochemical behaviour of cells assembled with aged electrodes was similar to the behaviour of fresh cells. For an examination of the effect of aging on porosity and surface area of the compound, S70 powder samples was soaked in $NaClO_4$ + PC electrolyte for about 7 days, washed with acetone and water, dried at 70 °C and N_2 adsorption-desorption isotherms as well as powder XRD patterns were recorded.

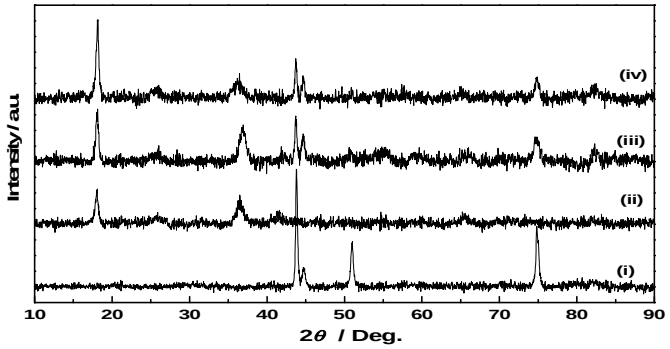

Fig. 7 XRD patterns for (i) SS mesh, (ii) electrode material consisting of MnO_2 (S70), AB and PTFE, (iii) electrode before charge-discharge cycle and (iv) electrode after charge-discharge cycling.

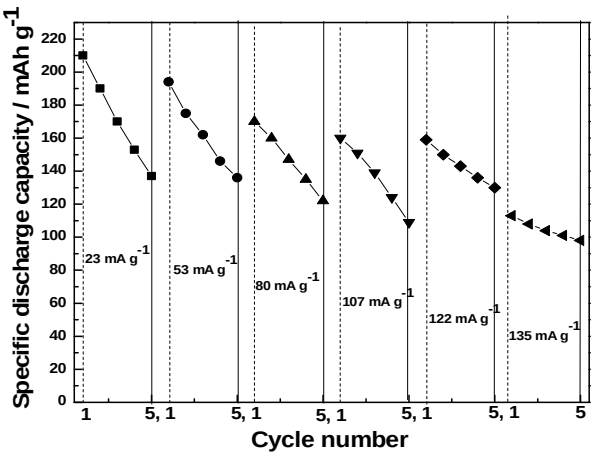

Fig. 8 Specific discharge capacity of MnO_2 sample (S70) at different current densities (i) 23, (ii) 53, (iii) 80, (iv) 107, (v) 122 and (vi) 135 mA g^{-1} for 5 cycles. A fresh electrode was used for each current.

The N_2 adsorption-desorption isotherm (Fig. 4h), surface area, porosity as well as the powder XRD pattern of the aged MnO_2 sample S70 were identical to those of fresh sample. Furthermore, the XRD pattern of cycled electrode (Fig. 8) is similar to the fresh electrode indicating that the amorphous MnO_2 (S70 sample) does not undergo a phase change on subjecting the electrode to repeated charge-discharge cycling. These observations suggest that the electrochemical cycling processes are responsible for capacity decay for the poorly crystalline samples.

The rate capability of S70 sample was studied by subjecting cells for charge-discharge cycles at different specific currents. Fresh cells were used for each specific current. The data are presented in Fig. 9. As expected, there is a decrease in discharge capacity on repeated cycling at each current. The initial discharge capacity is about 210 mAh g^{-1} at a specific current of 23 mA g^{-1}, it decreases with an increase of discharge current and it is about 120 mAh g^{-1} at a specific current of 135 mA g^{-1}. The high rate capability is attributed to porous nature of MnO_2 sample.

APPLICATIONS

MnO_2 has been prepared by dropwise mixing solutions of Mn^{2+} and Mn^{7+} ions. The method is very simple and can easily be scaled up for industrial synthesis of amorphous MnO_2. The first specific discharge capacity for amorphous samples are high and Na/MnO_2 primary batteries can be fabricated on similar line of Li/MnO_2 primary batteries.

CONCLUSIONS

Amorphous MnO_2 was prepared by redox reaction between aqueous solutions of $KMnO_4$ and $MnSO_4.H_2O$ at ambient conditions. The as prepared sample was amorphous and it had a specific surface area as high as 184 m^2 g^{-1} with well-defined and narrowly distributed mesopores of 3.5 nm pore diameter. On heating the samples between 300 and 800 °C, there was an increasing crystallinity into α-form and decreasing specific surface area with an increase in temperature. Na/MnO_2 cells were assembled in propylene carbonate electrolyte consisting of $NaClO_4$. The as prepared sample exhibited first discharge capacity of 194 mAh g^{-1} at a specific current of 50 mA g^{-1}. The attractively large value of discharge capacity of the as prepared amorphous MnO_2 was attributed to the large specific surface area and mesoporosity. There was a decrease in specific discharge capacity on subjecting the cells to repeated charge-discharge cycling. A discharge capacity of about 70 mAh g^{-1} was obtained at the end of 30 charge-discharge cycles. The initial discharge capacity values of crystalline α-MnO_2 samples were lower than the amorphous samples, but with improved cycling stability.

REFERENCES

[1] S.W. Kim, D.H. Seo, X. Ma, G. Ceder, K. Kang, *Adv. Energy Mater*, **2012**, 2, 710 – 721.
[2] V. Palomares, P. Serras, I. Villaluenga, K. B. Hueso, J. C. Gonzalez, T. Rojo, *Energy Environ. Sci.*, **2012**, 5, 5884–5901.
[3] V. Palomares, M.C. Cabanas, E.C. Martinez, M.H. Han, T. Rojo, *Energy Environ. Sci*, **2013**, 6, 2312–2337.
[4] C. Delmas, J.J. Braconnier, C. Fouassier, P. Hagenmuller, *Solid State Ionic*, **1981**, ¾, 165–169.
[5] L.W. Shacklette, T.R. Jow, L. Townsend, *J. Electrochem. Soc.*, **1988**, 135, 2669–2674.
[6] Caballero, L. Hernan, J. Morales, L. Sanchez, J. S. Pena, M. A. G Aranda, *J. Mater. Chem*, **2002**, 12, 1142 – 1147.
[7] N. Yabuuchi, M. Kajiyama, J. Iwatate, H. Nishikawa, S. Hitomi, R. Okuyama, R. Usui, Y. Yamada, S. Komaba, *Nat. Mater*, **2012**, 11, 512 – 517.
[8] D. Yuan, W. He, F. Pei, F. Wu, Y. Wu, J. Qian, Y. Cao, X. Ai, H. Yang, *J. Mater. Chem. A*, **2013**, 1, 3895 – 3899.
[9] P. Vassilaras, A.J. Toumar, G. Ceder, *Electrochem. Comm*, **2014**, 38, 79 – 81.
[10] Y. Deng, L. Wan, Y. Xie, X. Qin, G. Chen, *RSC Adv*, **2014**, 4, 23914 – 23935.
[11] T.T. Liu, G.J. Shao, M.T. Ji, Z.P. Ma, *Asian J. Chem*, **2013**, 25, 7065 – 7070.
[12] W. Wei, X. Cui, W. Chen, D.G. Ivey, *Chem. Soc. Rev*, **2011**, 40, 1697 – 1721.
[13] M.M. Doeff, M.Y. Peng, Y. Ma, L.C. De Jonghe, *J. Electrochem. Soc*, **1995**, 141, L145 – L147.
[14] F. Sauvage, L. Laffont, J.M. Tarascon, E. Baudrin, *Inorg. Chem*, **2007**, 46, 3289 – 3294.
[15] D. Su, H.J. Ahn, G. Wang, *J. Mater. Chem. A*, **2013**, 1, 4845 – 4850.
[16] H. Xiong, M.D. Slater, M. Balasubramanian, C.S. Johnson, T. Rajh, *J. Phys. Chem. Lett*, **2011**, 2, 2560–2565.
[17] G. Venkatesh, V. Pralong, O.I. Lebedev, V. Caignaert, P. Bazin, B. Raveau, *Electrochem. Commun*, **2014**, 40, 100 – 102.
[18] E. Uchaker, Y.Z. Zheng, S. Li, S.L. Candelaria, S. Hu, G.Z. Cao, *J. Mater. Chem. A*, **2014**, 2, 18208–18214.
[19] Y. Fang, L. Xiao, J. Qian, X. Ai, H. Yang, Y. Cao, *Nano Lett*, **2014**, 14, 3539–3543.
[20] C. Li, X. Miao, W. Chu, P. Wu, D.G. Tong, *J. Mater. Chem. A*, **2015**, 3, 8265–8271.
[21] H.Y. Lee, J.B. Goodenough, *J. Solid State Chem.*, **1999**, 144, 220–223.
[22] R.N. DeGuzman, Y.F. Shen, E.J. Neth, S.L. Suib, C.L. O'Young, S. Levine, J.M. Newsam, *Chem. Mater*, **1994**, 6, 815–821.
[23] Y. Chen, C. Liu, F. Li, H.M. Cheng, *J. Alloys Comp*, **2005**, 397, 282–285.
[24] X. Zhang, W. Yang, J. Yang, D.G. Evans, *J. Cryst. Growth*, **2008**, 310, 716–722.
[25] S.C. Pang, S.F. Chin, C.Y. Ling, *J. Nanomater*, **2012**, ID 607870.
[26] H. Xhao, Y. Dong, P. Jiang, G. Wang, J. Zhang, K. Li, C. Feng, *New J. Chem*, **2014**, 38, 1743–1750.
[27] S. Devaraj, N. Munichandraiah, *J. Phys. Chem. C*, **2008**, 112, 4406–4417.
[28] M.M. Thackeray, *Prog. Solid State Chem.*, **1997**, 25, 1–71.
[29] S.L. Brock, N. Duan, Z.R. Tian, O. Giraldo, H. Zhou, S.L. Suib, *Chem. Mater*, **1998**, 10, 2619 – 2628.
[30] Z. Huang, W. Zhou, C. Ouyang, J. Wu, F. Zhang, J. Huang, Y. Gao, J. Chu, *Sci. Rep*, **2015**, 5, 10899; doi: 10.1038/srep10899(2015).
[31] J. Kim, A. Manthiram, *Nature*, **1997**, 390, 265–267.
[32] J.J. Xu, G. Jain, J. Yang, *Electrochem. Solid-State Lett*, **2002**, 5, A152–A155.
[33] F. Leroux, L.F. Nazar, *Solid State Ionics*, **1997**, 100, 103–113.
[34] A.I. Palos, M. Anne, P. Strobel, *Solid State Ionics*, **2001**, 138, 203–212.
[35] Manthiram, J. Kim, *Chem Mater*, **1998**, 10, 2895–2909.
[36] J.J. Xu, A.J. Kisner, B.B. Owens, W.H. Smyrl, *Electrochem. Solid-State Lett*, **1998**, 1, 1–3.

[37] Y. Jiang, D. Zhang, Y. Li, T. Yuan, N. Bahlawane, C. Liang, W. Sun, Y. Lu, M. Yan, *Nano Energy*, **2014**, 4, 23 – 30.
[38] X. Zhau, R.K. Guduru, P. Mohanty, *J. Mater. Chem. A*, **2013**, 1, 2757–2761.

AUTHORS' ADDRESSES

1. **Mr. Brij Kishore**
Department of Inorganic and Physical Chemistry,
Indian Institute of Science, Bengaluru-560012, India.
Email:brij@ipc.iisc.ernet.in, Mobile- 09480329634
2. **Dr. Venkatesh Gopal**
Department of Instrumentation and Applied Physics
Indian Institute of Science, Bengaluru-560012, India.
Email:venkat81.g@gmail.com, Mobile- 08105386590
3. **Prof. Munichandraiah Nookala**
Department of Inorganic and Physical Chemistry,
Indian Institute of Science,Bengaluru-560012, India.
Email:muni@ipc.iisc.ernet.in, Contact: 080-2293-3183